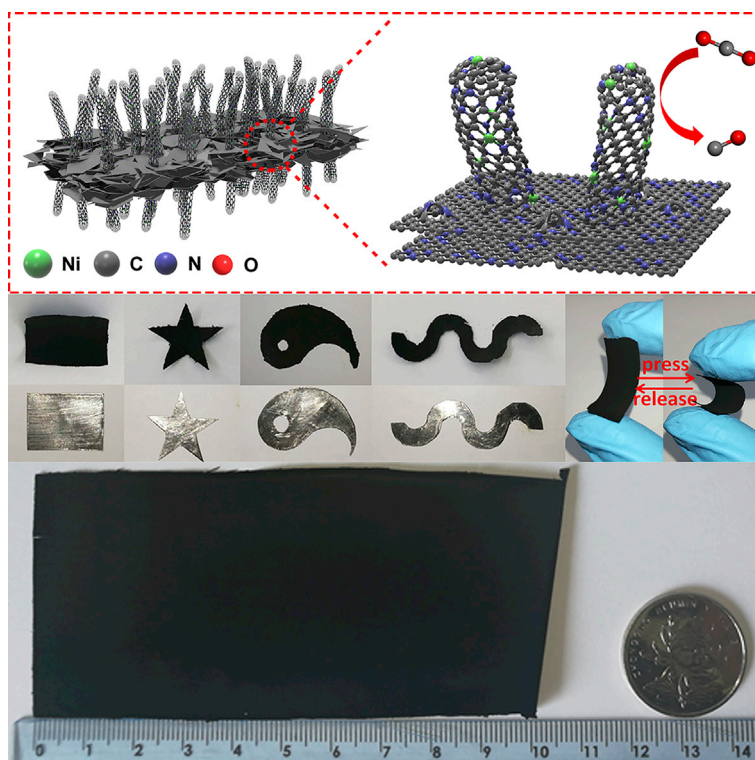


## Article

# Solid-Diffusion Synthesis of Single-Atom Catalysts Directly from Bulk Metal for Efficient CO<sub>2</sub> Reduction



Electroreduction of CO<sub>2</sub> into value-added products is an effective approach to remit the environmental and energy issues. In this study, a hierarchical, self-supported, and atomistic catalyst was successfully synthesized based on the solid-state diffusion strategy. This catalyst can be directly used as a binder-free electrode and exhibits superb catalytic CO<sub>2</sub> electroreduction performance. Directly synthesized by bulk metal foil, this catalyst is scalable to meet the industrial demand.

Changming Zhao, Yu Wang,  
Zhijun Li, ..., Haohong Duan,  
Yuen Wu, Yadong Li

liyafei@nynu.edu.cn (Y.L.)

haohong.duan@chem.ox.ac.uk (H.D.)

yuenwu@ustc.edu.cn (Y.W.)

## HIGHLIGHTS

Single Ni atoms coordinated in N-CNTs exhibit superb catalytic CO<sub>2</sub>RR performance

This catalyst can be directly used as an electrode toward the CO<sub>2</sub> electroreduction

This catalyst is programmable and scalable to meet the industrial demand

## Article

# Solid-Diffusion Synthesis of Single-Atom Catalysts Directly from Bulk Metal for Efficient CO<sub>2</sub> Reduction

Changming Zhao,<sup>1,11</sup> Yu Wang,<sup>4,11</sup> Zhijun Li,<sup>1</sup> Wenxing Chen,<sup>5</sup> Qian Xu,<sup>6</sup> Dongsheng He,<sup>7</sup> Desheng Xi,<sup>8</sup> Qinghua Zhang,<sup>9</sup> Tongwei Yuan,<sup>10</sup> Yunteng Qu,<sup>1</sup> Jian Yang,<sup>1</sup> Fangyao Zhou,<sup>1</sup> Zhengkun Yang,<sup>1</sup> Xiaoqian Wang,<sup>1</sup> Jing Wang,<sup>1</sup> Jun Luo,<sup>8</sup> Yafei Li,<sup>4,\*</sup> Haohong Duan,<sup>2,\*</sup> Yuen Wu,<sup>1,12,\*</sup> and Yadong Li<sup>3</sup>

## SUMMARY

**Electroreduction of CO<sub>2</sub> into value-added products is an effective approach to remit the environmental and energy issues. However, the development of an effective, accessible, and simple method for mass production of electrocatalyst is challenging. Herein, we demonstrate the solid-state diffusion between the N-doped carbon phase and bulk Ni metal can be utilized to synthesize hierarchical, self-supported, and atomistic catalyst. Strikingly, this hierarchical catalyst is programmable and scalable to meet the industrial demand and can be directly used as a binder-free electrode toward the CO<sub>2</sub> electroreduction, delivering a state-of-the-art current density of 48.66 mA cm<sup>-2</sup> at -1.0 V versus reversible hydrogen electrode (RHE) and high faradic efficiency of 97% to CO. The selectivity can be retained over 90% in a wide range of working potential of -0.7 to -1.2 V versus RHE. This solid-state diffusion strategy presents great potential to produce hierarchical and atomistic catalysts at industrial levels.**

## INTRODUCTION

In the aim of achieving the desired chemical and physical properties, solid-state diffusion has been widely used to engineer microstructures of functional intermetallics and alloys such as composition, crystal phase, and grain boundary for more than half a century.<sup>1–3</sup> Notable examples have been reported in a diverse range of areas including catalytic performance,<sup>4,5</sup> ferromagnetism,<sup>6</sup> conductivity,<sup>7</sup> shape-memory effects, and so on.<sup>8</sup> The directional material and interface flows are affected by differential solid-state diffusion rates of the diffusion couple at high temperature, i.e., copper and zinc in brass.<sup>9</sup> For the solid-state materials such as heterogeneous catalysts, the microstructures which determine their size- and shape-dependent properties in advanced applications are very sensitive to the synthetic conditions.<sup>10,11</sup> Moreover, the ability to manipulate the structure of solid materials at nano even atomic levels would greatly modulate the local chemical environment and enhance the corresponding properties.<sup>12,13</sup> However, this old method is not generally considered as an effective method of preparing solid materials with sophisticated atomistic structures due to poor control over the drastic reaction at high temperature.

The excessive emission of greenhouse gas CO<sub>2</sub> through massive fossil fuel consumption results in serious environmental issues.<sup>14</sup> There is an urgent need to convert CO<sub>2</sub> into chemical fuels to mitigate atmospheric CO<sub>2</sub> level and alleviate the energy crisis.<sup>15,16</sup> An ideal catalyst for CO<sub>2</sub> electroreduction should comprise

## Context & Scale

The excessive emission of CO<sub>2</sub> through massive fossil fuel consumption results in serious environmental issues. There is an urgent need to convert CO<sub>2</sub> into chemical fuels to mitigate atmospheric CO<sub>2</sub> levels and alleviate the energy crisis. Therefore, the design and synthesis of high-performance and flexible self-supported electrocatalysts for CO<sub>2</sub> reduction are highly desirable to realize high-efficiency practical devices. Herein, we successfully synthesize a hierarchical and atomistic catalyst through a solid-state diffusion strategy. This synthesis is initiated by the direct solid-state diffusion of Ni atoms from bulk Ni foil into the contacted carbon shell. Catalyzed by the Ni “seeds” derived from the bulk Ni, self-supported nanotube fiber-based carbon paper decorated by abundant isolated atomistic Ni sites are successfully “cultivated.” This hierarchical catalyst is programmable and scalable to meet the industrial demand for CO<sub>2</sub> conversion.

sufficient accessible surface, highly reactive sites, and reliable steadiness to meet industrial demand, including high working overpotential, high current density to target products, and easy development to large production. Moreover, to reach industrial-scale electrodes, most of the previously reported catalysts for CO<sub>2</sub> electroreduction have to be fixed on a conductive substrate with the help of insulating polymer binders, such as Nafion or PVDF,<sup>17</sup> which largely increases the synthetic complexity and cost. To satisfy the industrial requirements mentioned above, developing a scalable approach that can transform the inexpensive raw materials such as bulk metal into efficient and stable catalysts is highly needed.

## RESULTS AND DISCUSSION

### Synthesis and Characterization

Herein, we describe an effective approach to construct a hierarchical and atomistic catalyst by the solid-state diffusion between the bulk Ni and N-doped carbon (N-C) layer. Especially, this carbon paper is self-supported and can be directly used as a binder-free electrode for CO<sub>2</sub> reduction. In line with other reported rough surfaces in MoS<sub>2</sub>,<sup>18</sup> Ni<sub>2</sub>Co<sub>1</sub>@Ni<sub>2</sub>Co<sub>1</sub>O<sub>x</sub>,<sup>19</sup> and Cu films,<sup>20</sup> the as-prepared carbon paper possesses a large surface with both superhydrophilic and superaerophobic properties, which is a benefit for the contact of dissolved CO<sub>2</sub> and the desorption of generated CO. In addition, the abundant single-Ni sites distributing on the catalyst's surface also play a dominant impact on the activation of CO<sub>2</sub>.<sup>21,22</sup>

A mechanism illustrating the programmable formation process of the catalyst is summarized in Figure 1A. Firstly, the melamine was deposited onto the Ni foil surface by spray painting equipment to form a thin film. By precisely controlling the heating rate from room temperature to 1,000°C, the melamine film was gradually converted to a C<sub>3</sub>N<sub>4</sub> structure,<sup>23</sup> covering over the Ni foil. The C<sub>3</sub>N<sub>4</sub> can be converted to N-C at high temperature catalyzed by Ni source.<sup>24</sup> Driven by a strong Lewis acid-base interaction between Ni-N coordination, the abundant unsaturated carbon vacancies formed at high temperature allowed the surface Ni atoms to diffuse into the covered N-C soil and occupy the carbon vacancies. Meanwhile, this directional material flow of Ni from Ni foil into the N-C layer was balanced by an opposite flow of C into the Ni foil. The Ni NPs acted as seeds to germinate nitrogen-doped carbon nanotubes (N-CNT) by a vapor-liquid-solid mechanism,<sup>25</sup> when the C was supersaturated in the metal particles, C precipitation at the rear of the metal droplet occurred and the droplet was located on the top of growing nanotube.<sup>26,27</sup> The C<sub>3</sub>N<sub>4</sub> would vaporize at a continuous high temperature to give C and N sources for the growth of carbon tubes.<sup>23</sup> Catalyzed by the Ni "seeds" derived from the bulk Ni, N-CNTs were cultivated on the surface of N-C layer to obtain a hierarchical structure (Figures 1B, 1C, and S1), in which the as-grown one-dimensional nanotube are perpendicular to the two-dimensional N-C layer. The cross-sectional scanning electron microscope (SEM) images (Figure 1B) and the corresponding energy-dispersive X-ray spectroscopy (EDS) mapping images (Figure 1D) both confirm the hierarchical structure and the diffusion of Ni NPs into the N-C soil from the bulk Ni foil. These flexible and free-standing carbon papers can be easily peeled off from the Ni foil surface to form freshly prepared carbon papers (F-CPs). Finally, after an acid-leaching step to dissolve a majority of Ni seeds within the N-C soil, hierarchical carbon papers (H-CPs) with abundant N-CNT on both sides were obtained (Figures 1E and S2). As revealed by Figure S3, the rigorous encapsulation within a few layer of graphene would result in some residual Ni crystals by cutting off the interaction between Ni and proton.<sup>21,28</sup> Aberration-corrected high-angle annular dark-field scanning transmission electron microscopy (HAADF-STEM) images (Figures 1F and 1G) of

<sup>1</sup>Department of Chemistry, Hefei National Laboratory for Physical Sciences at the Microscale, iChEM (Collaborative Innovation Center of Chemistry for Energy Materials), University of Science and Technology of China, Hefei 230026, China

<sup>2</sup>Chemistry Research Laboratory, Department of Chemistry, University of Oxford, 12 Mansfield Road, Oxford OX1 3TA, UK

<sup>3</sup>Department of Chemistry, Tsinghua University, Beijing 100084, China

<sup>4</sup>Jiangsu Collaborative Innovation Centre of Biomedical Functional Materials, School of Chemistry and Materials Science, Nanjing Normal University, Nanjing 210023, China

<sup>5</sup>Beijing Key Laboratory of Construction Tailorable Advanced Functional Materials and Green Applications, School of Materials Science and Engineering, Beijing Institute of Technology, Beijing 100081, PR China

<sup>6</sup>National Synchrotron Radiation Laboratory (NSRL), Hefei 230026, China

<sup>7</sup>Materials Characterization and Preparation Center (MCPC), Southern University of Science and Technology (SUSTech), 1088 Xueyuan Road, Shenzhen 518055, PR China

<sup>8</sup>Institute for New Energy Materials & Low-Carbon Technologies, Tianjin University of Technology, Tianjin 300384, China

<sup>9</sup>Institute of Physics, Chinese Academy of Sciences, Beijing 100190, PR China

<sup>10</sup>NEST Lab, Department of Chemistry, College of Science, Shanghai University, Shanghai 200444, PR China

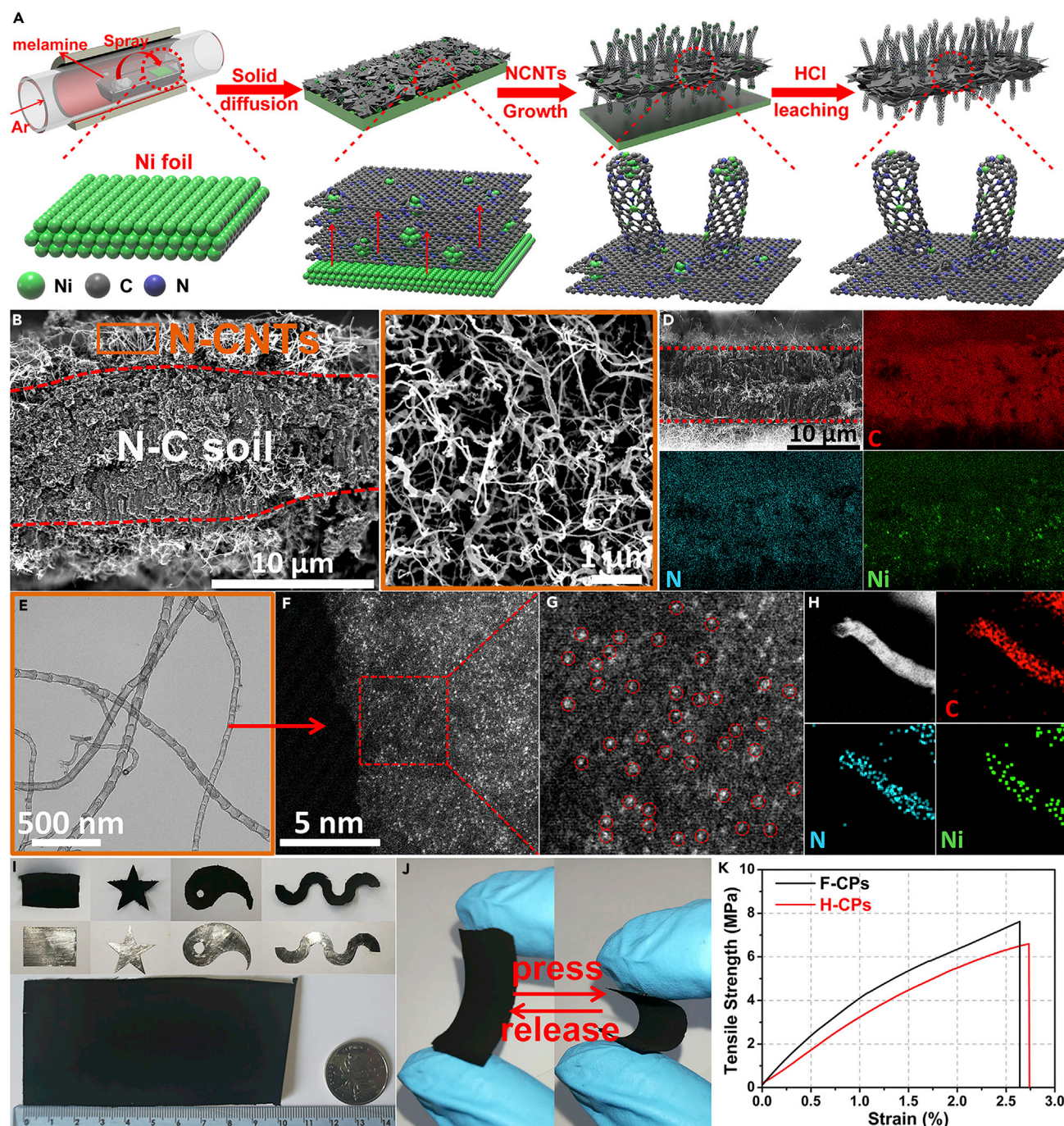
<sup>11</sup>These authors contributed equally

<sup>12</sup>Lead Contact

\*Correspondence: liyafei@njnu.edu.cn (Y.L.), haohong.duan@chem.ox.ac.uk (H.D.), yuenwu@ustc.edu.cn (Y.W.)

<https://doi.org/10.1016/j.joule.2018.11.008>





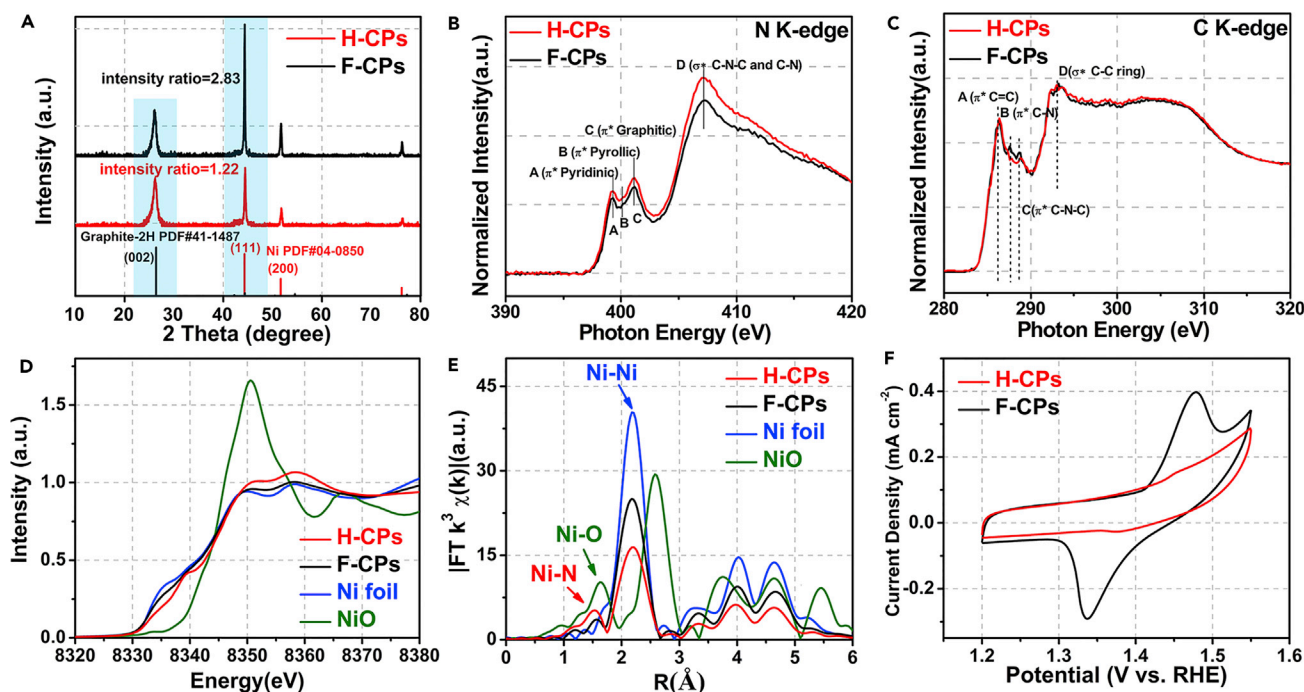


**Figure 2. Characterizations of H-CPs**

(A) XRD patterns of H-CPs and F-CPs.  
(B and C) N K-edge (B) and C K-edge (C) NEXAFS spectra of H-CPs and F-CPs.  
(D and E) Ni K-edge XANES spectra (D) and  $k^3$ -weighted  $\chi(k)$  function of the EXAFS spectra (E).  
(F) CV curves in 0.1 M KOH electrolyte at a scan rate of 5 mV s<sup>-1</sup>.

H-CPs show that the Ni atoms dominantly presented an atomic dispersion over the surface of nanotube, demonstrating their robust resistance to acid leaching.<sup>29–31</sup> The isolated heavier Ni single atoms (SAs) could be discerned in the carbon support because of the different Z contrasts among Ni, N, and C.<sup>32</sup> The Ni and N were homogeneously dispersed on the N-CNTs, as demonstrated by EDS analysis (Figure 1H). Importantly, the whole synthetic procedure is programmable so that the areas and shape of the H-CPs is strictly determined by the bulk Ni foil substrate (Figure 1I). To fulfill the industrial production requirements, this flexible and self-supported H-CPs is easy to be massively manufactured according to the standard steps, and the Ni foil can be reused after removing the surface carbide by a simple polishing treatment, which is shown in Video S1. As shown in Figure 1J and Video S1, the H-CP is as robust and flexible as the commercial carbon cloth, since it can retain the paper structure under bending stress to some extent. It also can tolerate more than 6 MPa tensile strength, as revealed by the stress-strain curves in Figure 1K. Due to the excellent mechanical properties, the H-CPs can be directly assembled as an electrode for CO<sub>2</sub> electrochemical reduction, without the addition of binder and support.

As shown by X-ray powder diffraction (XRD) patterns in Figure 2A, the F-CPs showed typical mixed crystal patterns including Ni nanoparticles (NPs) and graphene. After acid treatment, the peak intensity assigned to the crystalline Ni clearly decreased, in line with transmission electron microscopy (TEM) observations. To investigate the electronic structure of the catalysts, near-edge X-ray absorption fine structure (NEXAFS) measurements were performed. For the N K-edge spectrum (Figure 2B), peak A (399.5 eV) and peak C (402.4 eV) can be assigned to pyridinic  $\pi^*$  and



graphitic  $\pi^*$  transitions in H-CPs and F-CPs, respectively. Peak D (408.5 eV) suggests the formation of C–N–C or C–N  $\sigma^*$  bond. For the C K-edge spectrum (Figure 2C), peak A (285.6 eV) derived from C=C  $\pi^*$  (ring) excitations, and peak D (293.2 eV) originated from C–C  $\sigma^*$  (ring) transitions. These results strongly support the idea that acid treatment does not damage the skeleton structure of the N-C support but instead dissolves most of the Ni crystals, which can also be confirmed by the unchanged  $I_D/I_G$  value at Raman spectra (Figure S4). More detailed structural information was obtained from X-ray absorption fine structure (XAFS). As shown in the X-ray absorption near-edge structure (XANES) spectra of H-CPs (Figure 2D), the intensity of the line located between those of the Ni foil and NiO clearly display the unique electronic structure of  $Ni^{\delta+}$  ( $0 < \delta < 2$ ). Compared with the F-CPs, the Fourier transform  $k^3$ -weighted  $\chi(k)$  function of the EXAFS spectra for H-CPs indicated the dominating Ni–Ni bonding (at 2.15 Å) significantly decreased and a new Ni–N coordination at 1.42 Å appeared (Figure 2E). Combined with XRD and TEM findings, these results suggest that the majority of Ni NPs could be removed after a chemical etching process in diluted HCl, leaving a small amount of Ni NPs encapsulated within the multiwall carbon nanotube. Reinforced by the cyclic voltammetry (CV) curves measurements in N<sub>2</sub>-saturated alkaline media (Figure 2F), the disappeared Ni reduction/oxidation redox peaks corroborate that the exposed Ni crystals were largely leached, mainly leaving the single coordinated Ni species.<sup>33</sup> The surface-sensitive technology of X-ray photoelectron spectroscopy was used to characterize the valence state and composition evolution during the synthetic process (Figures S5 and S6). After the acid treatment, a higher proportion of ionic  $Ni^{\delta+}$  ( $0 < \delta < 2$ ) species can be found for the H-CPs with respect to unleached F-CPs, since the single  $NiN_x$  dominantly occupy the surface and the most of Ni(0) are dissolved.<sup>30,34</sup> As shown by the Brunauer-Emmett-Teller measurements in Figure S7, the H-CPs inherited a higher surface area of 143.97 m<sup>2</sup> g<sup>−1</sup> than that of F-CPs (113.21 m<sup>2</sup> g<sup>−1</sup>) because of the dissolution Ni NPs. This enhancement in specific surface area could result in an increased CO<sub>2</sub> adsorption capacity from 3.85 to 7.64 cm<sup>3</sup> g<sup>−1</sup> at 100 kPa, as verified by the CO<sub>2</sub> adsorption isotherms.

### Evaluation of Activity for Electrochemical Reduction of CO<sub>2</sub>

The CO<sub>2</sub> electroreduction was performed in a two-compartment gas-tight cell, which was separated by a Nafion-115 proton exchange membrane to prevent the oxidation of as-generated products. The cathodic compartment was continuously purged with CO<sub>2</sub> (20 mL min<sup>−1</sup>) and vented directly into the gas-sampling loop (0.5 mL) for the periodic quantification of the gas-phase products by gas chromatography (GC). Liquid products were analyzed by <sup>1</sup>H NMR spectroscopy after electrochemical CO<sub>2</sub> reduction processes. The comparison of the CO<sub>2</sub> reduction activity for F-CPs and H-CPs is summarized in Figure 3. Linear sweep voltammetry measurements (Figure 3A) for F-CPs and H-CPs were conducted in N<sub>2</sub>-saturated 0.5 M NaClO<sub>4</sub> solution and CO<sub>2</sub>-saturated 0.5 M KHCO<sub>3</sub> solution to exclude the influence of HCO<sub>3</sub><sup>−</sup>. The H-CPs showed a much higher activity in CO<sub>2</sub>-saturated KHCO<sub>3</sub> solution with a low onset potential of −0.32 V versus a reversible hydrogen electrode (RHE) (all potentials are with reference to the RHE). In addition, the specific CO current density catalyzed by H-CPs reached a high value of 60.11 mA cm<sup>−2</sup> at −1.2 V, almost seven times higher than that for F-CPs (Figure S8). The H-CPs maintain excellent faradic efficiency (FE) in a wide range of working potentials from −0.7 to −1.2 V (the FE of CO is over 90.8%), which indicates that the competitive hydrogen evolution reaction (HER) is largely prohibited over the single Ni sites. The primary products catalyzed by the H-CPs and F-CPs are CO and H<sub>2</sub> (Figure S9), and no liquid product is detected by <sup>1</sup>H NMR (Figure S10). As revealed by Figure 3C, the Tafel slope of H-CPs is 105 mV/decade, much smaller than that of F-CPs (136 mV/decade),

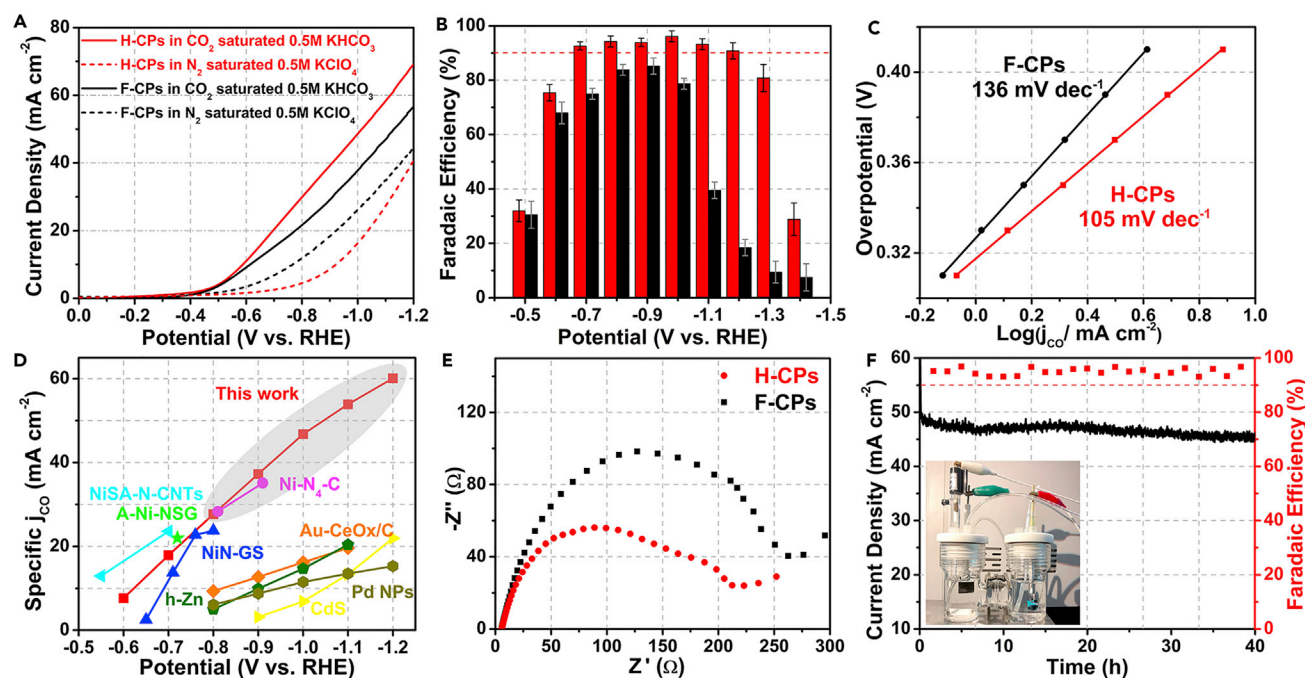


**Figure 3. Performance of CO<sub>2</sub> Electroreduction**

(A) Linear sweep voltammetry curves in N<sub>2</sub>-saturated (dotted line) 0.5 M KClO<sub>4</sub> or CO<sub>2</sub>-saturated (solid line) 0.5 M KHCO<sub>3</sub> electrolyte at a scan rate of 10 mV s<sup>-1</sup>.  
 (B and C) (B) FEs of CO and (C) Tafel plot of the partial CO current density for H-CPs (red) and F-CPs (black) at different applied potentials.  
 (D) Specific current density of H-CPs compared with those of other state-of-the-art catalysts for CO<sub>2</sub> to CO reduction (highlighted in the high potential region).  
 (E) Nyquist plots for H-CPs and F-CPs.  
 (F) Stability test of H-CPs at a potential of -1.0 V versus RHE during 40 hr.

indicating more favorable kinetics for the formation of CO.<sup>35</sup> Accounting for the reduction of CO<sub>2</sub> to CO, this catalytic behavior outperforms most of the previously reported catalysts to the best of our knowledge (Figure 3D; Table S1), especially at high current density. Nyquist plots reveals that H-CPs have a lower interfacial charge-transfer resistance ( $R_{CT}$ ) than F-CPs (Figure 3E), hence ensuring faster electron transfer from the electrodes to CO<sub>2</sub> and favorable formation of the CO<sub>2</sub><sup>•-</sup> radical anion intermediate. Strikingly, the H-CPs also exhibited a long-term stability over 40-hr operations at -1.0 V, without obvious decay in both FE and current density (Figure 3F). As revealed in Figure S11, a plot of  $\log(j_{CO})$  versus  $\log([HCO_3^-])$  shows a slope of 0.96, demonstrating that the HCO<sub>3</sub><sup>-</sup> concentration greatly influences the efficiency of electrochemical CO<sub>2</sub> reduction. The HCO<sub>3</sub><sup>-</sup> may not only simply act as a pH buffer and proton donor in the reaction, but also increase the concentration of CO<sub>2</sub> near the electrode surface via rapid equilibrium with bicarbonate.<sup>36,37</sup> Interestingly, the current density of Ni foil and Ni NPs/C was even lower in the CO<sub>2</sub>-saturated electrolyte than in the N<sub>2</sub>-saturated electrolyte (Figure S12). This confirmed that the surface of the Ni bulk may be poisoned by the generated CO to further restrict the HER.<sup>38</sup> The CV measurements (Figure 2F) further confirmed that the Ni NPs in H-CPs was protected by the graphene shell and cannot directly contact with the solution.<sup>33</sup> There is no evidence to demonstrate the Ni NPs be directly in contact with the electrolyte to be involved in the gas reduction reactions.<sup>21</sup> It has documented that the SCN<sup>-</sup> ion has a high affinity to nickel and thus can poison the isolated Ni single-atom sites.<sup>31</sup> As shown in Figure S13, a significant depression of catalytic activity for H-CPs is observed, which could be attributed to

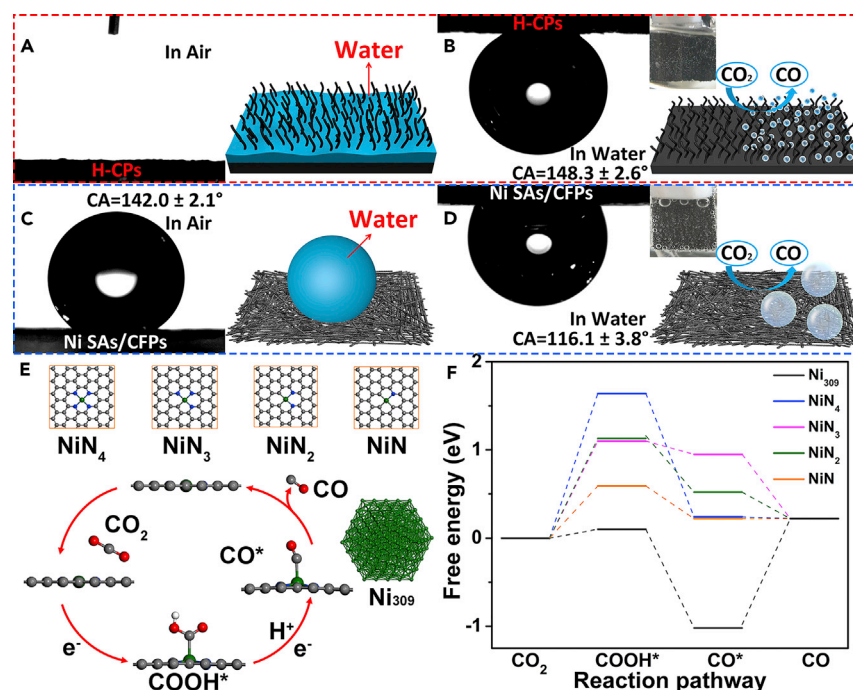


**Figure 4. Schematic and Contact Angles of H-CPs, and DFT Studies of CO<sub>2</sub> Electroreduction**

(A and C) The water contact angles and schematic illustration of H-CPs (A) and Ni SAs/CFPs (C). (B and D) Underwater gas bubble contact angles and schematic illustration of H-CPs (B) and Ni SAs/CFPs (D).

(E) Optimized atomic structures of Ni<sub>309</sub> cluster, different NiN<sub>x</sub> structures, and proposed reaction paths for CO<sub>2</sub> electroreduction by H-CPs. C, O, Ni, N, and H atoms are represented by gray, red, green, blue, and white spheres, respectively.

(F) Free energy diagram for the conversion of CO<sub>2</sub> to CO on the Ni SAs and Ni<sub>309</sub> cluster at U = 0 V versus RHE.

the blocking effect of SCN<sup>−</sup> on single Ni sites. Hence, it is reasonable to attribute the dominant impact on the high activity and selectivity to the exposed isolated Ni sites. To further demonstrate that Ni SAs were active sites, Ni NPs encapsulated by the graphitic carbons (Ni NPs@GC) were prepared. The results show these Ni NPs encapsulated by the multilayered graphene (Figure S14) present nearly no activity toward CO formation (Figure S15). In addition, the CO<sub>2</sub> electroreduction activity of H-CPs was evaluated onto a gas diffusion layer electrode in a flow cell configuration (Figures S16 and S17) using 1.0 M KOH and CO<sub>2</sub>-saturated 1.0 M KHCO<sub>3</sub> electrolyte (Figures S18–S20), where a CO partial current of 91.1 mA cm<sup>−2</sup> was obtained at 3.0 V cell voltage.

### Computational Studies and Further Research

The vertically aligned structure of N-CNTs provided not only excellent conductivity but also large contact area for ion diffusion due to the superhydrophilic and super-aerophobic surface. The superhydrophilic structure is benefited for mass transfer by electrolyte-wetting on the catalyst's surface, and the superaerophobic surface can facilitate the removal of an as-formed gas product within the bubbles, especially at high reaction rates.<sup>18,20</sup> As shown in Figure 4A, the water contact angle (CA) of H-CPs was nearly 0°, showing the outstanding wetting property of the surface constituting vertically aligned carbon nanotubes. The rough nanostructured surface could significantly reduce the adhesion force between electrode surface and gas bubbles. Meanwhile, the CA of the gas bubble on this surface in aqueous solution was



measured to be  $148.3^\circ \pm 2.6^\circ$ , implying the excellent superaerophobic property. As shown in [Video S1](#), the generated bubbles quickly disappear before they grew larger without stirring, which is conducive to the real industrial operation. To better evaluate the impact of superhydrophilic and superaerophobic surface on the catalytic performance, we directly load the N-doped carbon decorated by Ni SAs on commercial carbon fiber papers (Ni SAs/CFPs) as a control sample. Without the vertically aligned array structure ([Figure S21](#)), the water and gas CA of Ni SAs/CFPs are  $142.0^\circ \pm 2.1^\circ$  and  $116.1^\circ \pm 3.8^\circ$ , respectively, which is detrimental to the desorption of the gas product. In spite of the same catalyst loading, the current density delivered by Ni-N-C/CFPs is significantly inferior to that of H-CPs under the same potential ([Figure S22](#)).

The differences in activity between Ni in single-atom and non-single-atom states toward CO<sub>2</sub>RR were further understood using spin-polarized density functional theory (DFT) calculations. Here, the activity center of Ni SAs was modeled as various NiN<sub>x</sub> moieties (x = 1–4) embedded in a graphene nanosheet while the Ni NPs were represented by a Ni<sub>309</sub> cluster (see computational details and [Figure 4E](#)). We first studied the O\* formation and OH\* removal on the Ni systems, since these intermediates (occupation of active sites) are required to be cleared before CO<sub>2</sub>RR. Compared with the Ni<sub>309</sub> cluster that is prone to oxidation with an O\* formation free energy ( $\Delta G_{O^*}$ ) of  $-0.16$  eV, the Ni sites of NiN<sub>4</sub>, NiN<sub>3</sub>, NiN<sub>2</sub>, and NiN are more oxidation resistant ( $\Delta G_{O^*} = 4.35, 1.90, 1.80$ , and  $0.62$  eV, respectively). Besides, in sharp contrast to Ni<sub>309</sub> cluster which requires a potential of  $-0.31$  V to remove the adsorbed OH, the four Ni SAs do not need an additional potential to remove OH\* because these processes are considerably exothermic ( $\Delta G$ :  $-1.66$  eV for NiN<sub>4</sub>,  $-1.35$  eV for NiN<sub>3</sub>,  $-1.47$  eV for NiN<sub>2</sub>, and  $-1.19$  eV for NiN).

The adsorption free-energies of CO<sub>2</sub>RR intermediates ([Table S2](#)) and the reaction free-energies ( $\Delta G$ ) of elementary steps for all studied systems were then calculated employing the computational hydrogen electrode model.<sup>39</sup> The corresponding free energy profiles of all five systems are summarized in [Figure 4F](#), and the proposed reaction paths of CO<sub>2</sub>RR on NiN<sub>x</sub> are also displayed. According to our calculations, the reduction of CO<sub>2</sub> to COOH\* on the surfaces of all five systems are uphill in the free energy profiles, revealing that the first electronic step (CO<sub>2</sub> activation) is the potential-limiting step for both Ni SAs and Ni NPs. Especially, the Ni<sub>309</sub> cluster has the most favorable  $\Delta G$  ( $0.1$  eV) for this step, followed by NiN ( $0.59$  eV), NiN<sub>3</sub> ( $1.10$  eV), NiN<sub>2</sub> ( $1.11$  eV), and NiN<sub>4</sub> ( $1.64$  eV). The formed COOH\* species can be easily reduced to a CO\* species for both NiN<sub>x</sub> and Ni<sub>309</sub> clusters with the help of a proton coupled with an electron transfer. For four kinds of NiN<sub>x</sub>, the steps of CO\* desorption all have a negative  $\Delta G$ , indicating that the formed CO\* species can be effectively removed from the surface of the catalyst to complete the reduction. In sharp contrast, the CO\* desorption from the Ni<sub>309</sub> cluster is rather difficult ( $\Delta G = 1.13$  eV) due to the rather strong binding strength of CO\*, which is rather unfavorable for an efficient catalyst. Therefore, our calculations revealed that Ni NPs would show a much poorer catalytic performance than Ni SAs toward CO<sub>2</sub> reduction to CO. Considering that several Ni atoms of H-CPs may feature dimer or trimer states, we then studied the CO<sub>2</sub> reduction over the Ni dimer and trimer sites, and five types of activity center are accordingly constructed ([Figure S23](#)). After exploring the free energy changes along the reaction path, it is found that, although Ni dimer and trimer can well fulfill the conversion of CO<sub>2</sub> to COOH\*, their subsequent CO desorption steps generally are energetically unfavorable. Hence, the Ni dimer and trimer should not contribute to CO formation.

The HCOO\* pathway on the NiN<sub>x</sub> was further simulated. As shown in Figure S24, NiN<sub>4</sub>, NiN<sub>2</sub>, and NiN prefer the COOH\* pathway, whereas NiN<sub>3</sub> is slightly prone to HCOO\* formation. Another pathway, direct dissociation of CO<sub>2</sub>, was not explored in this work because it is generally difficult under the mild electrochemical environment, and there is no available active site near the single-atom Ni to accommodate the dissociated CO\* or O\*. We also performed DFT calculations to access the HER activity of NiN<sub>x</sub> via calculating their adsorption free energy of \*H species ( $\Delta G_{H^*}$ ). According to our calculations, NiN<sub>4</sub> has an impressive positive  $\Delta G_{H^*}$  of 1.52 eV, whereas the chemical adsorption of H\* is not stable on the single-atom Ni sites of the rest of NiN<sub>x</sub>. Therefore, competitive H<sub>2</sub> production would be significantly suppressed over all four single-atom Ni sites, which confirms the experimentally observed preferential CO<sub>2</sub>RR over HER (Figure 3). Moreover, we find that the  $\Delta G_{H^*}$  of the Ni<sub>309</sub> cluster is −0.37 eV, implying that Ni would be more prone to H<sub>2</sub> formation if it is not in the single-atom state (Figure S15).

The generality of this method was validated by construction of a cobalt single-atom catalyst supported on H-CPs under identical conditions. Similar H-CPs, with carbon nanotubes perpendicular to the N-C layer, were manifested by cross-section SEM (Figure S25) and EDS mapping (Figures S26 and S27). The aberration-corrected HAADF-STEM (Figure S28) and EXAFS spectra (Figure S29) both demonstrated the atomically dispersed cobalt atoms stabilized on H-CPss.

In summary, we prepared a self-supported, flexible, and programmable H-CPss catalyst containing abundant single Ni sites by a solid-state diffusion between the loose N-doped carbon phase and a compact bulk Ni metal. This catalyst can be directly used in CO<sub>2</sub> electroreduction without the use of conductive substrate and insulating polymer binders. The FE of CO maintained over 90% in a wide range of working potentials (−0.7 to −1.2 V). Together, this approach shed light to the construction of efficient and stable catalyst directly from the non-precious bulk materials and show great promise for industrial-scale production.

## EXPERIMENTAL PROCEDURES

### Synthesis of F-CPs

In a typical procedure, 2.0 g melamine was mixed with 4 mL deionized (DI) water under ultrasonic dispersing to get a homogeneous ink. A total of 200 mg cm<sup>−2</sup> melamine was evenly sprayed on a Ni foil substrate using an air brush. After being dried in a vacuum chamber, the sample was placed in a porcelain boat (as shown in Video S1) and placed in a tube furnace and heated at 1,000°C for 2 hr (heating rate 10°C/min) in a stream of Ar (10 mL/min). After the temperature was naturally cooled down to room temperature, the black carbon paper peeled off automatically from the Ni foil surface. The shape of the carbon paper can be controlled by the shape of the Ni foil, which can be reused for several times after polishing.

### Synthesis of H-CPs

The as-prepared F-CPs was treated in 3.0 mol/L HCl solution for 4 hr, then sample rinsed with 0.5 M KHCO<sub>3</sub> solution and DI water three times to remove residual HCl. Finally, the sample was dried and can be directly used for further tests.

All other experimental and setup details, as well the DFT calculations, are provided in the Supplemental Experimental Procedures.

## SUPPLEMENTAL INFORMATION

Supplemental Information includes Supplemental Experimental Procedures, 30 figures, 2 tables, and 1 video and can be found with this article online at <https://doi.org/10.1016/j.joule.2018.11.008>.

## ACKNOWLEDGMENTS

This work was supported by the National Key R&D Program of China 2017YFA (0208300) and (0700100) and the National Natural Science Foundation of China (21522107, 21671180, 21521091, U1463202, and 21873050). We thank the photoemission endstations BL1W1B in Beijing Synchrotron Radiation Facility (BSRF), BL14W1 in Shanghai Synchrotron Radiation Facility (SSRF), and BL10B and BL11U in National Synchrotron Radiation Laboratory (NSRL) for the help in characterizations.

## AUTHOR CONTRIBUTIONS

Y. Wu. conceived the idea and co-wrote the paper. C.Z. and Y. Wang. contributed equally to this work. C.Z. and F.Z. carried out the sample synthesis, characterization, and CO<sub>2</sub> electroreduction measurement. Y. Wang. and Y.L. carried out the theoretical calculations. Z.L., Y.Q., T.Y., J.Y., Z.Y., X.W., H.D., and Y.L. helped with the modification of the paper. Q.X. performed the NEXAFS experiments. D.X. and J.L. performed the SEM experiments. W.C. helped with the XAFS measurements and discussion. Q.Z. helped with the spherical aberration electron microscopy tests. All authors participated in the discussion of the results, commented on the implications, and fully approved the content of the manuscript.

## DECLARATION OF INTERESTS

The authors declare no competing interests.

Received: June 10, 2018

Revised: September 28, 2018

Accepted: November 9, 2018

Published: December 5, 2018

## REFERENCES

1. Reed-Hill, R.E., Abbaschian, R., and Abbaschian, R. (1973). *Physical Metallurgy Principles* (Van Nostrand).
2. Flemings, M.C. (1991). Behavior of metal alloys in the semisolid state. *Metall. Trans. A* 22, 957–981.
3. Mehrer, H. (2007). *Diffusion in Solids: Fundamentals, Methods, Materials, Diffusion-Controlled Processes* (Springer Science & Business Media).
4. Huang, X., Zhao, Z., Cao, L., Chen, Y., Zhu, E., Lin, Z., Li, M., Yan, A., Zettl, A., and Wang, Y.M. (2015). High-performance transition metal-doped Pt<sub>3</sub>Ni octahedra for oxygen reduction reaction. *Science* 348, 1230–1234.
5. Li, M., Zhao, Z., Cheng, T., Fortunelli, A., Chen, C.-Y., Yu, R., Zhang, Q., Gu, L., Merinov, B.V., and Lin, Z. (2016). Ultrafine jagged platinum nanowires enable ultrahigh mass activity for the oxygen reduction reaction. *Science* 354, 1414–1419.
6. Sun, S., Murray, C.B., Weller, D., Folks, L., and Moser, A. (2000). Monodisperse FePt nanoparticles and ferromagnetic FePt nanocrystal superlattices. *Science* 287, 1989–1992.
7. Cava, R., Takagi, H., Zandbergen, H., Krajewski, J., Peck, W., Jr., Siegrist, T., Batlogg, B., Van Dover, R., Felder, R., and Mizuhashi, K. (1994). Superconductivity in the quaternary intermetallic compounds LnNi<sub>2</sub>B<sub>2</sub>C. *Nature* 367, 252.
8. Funakubo, H., and Kennedy, J. (1987). *Shape Memory Alloys* (Gordon and Breach), xii + 275 pp.
9. Smigelskas, A., and Kirkendall, E. (1947). Zinc diffusion in alpha brass. *Trans. AIME* 171, 130–142.
10. Bi, Y., Ouyang, S., Umezawa, N., Cao, J., and Ye, J. (2011). Facet effect of single-crystalline Ag<sub>3</sub>PO<sub>4</sub> sub-microcrystals on photocatalytic properties. *J. Am. Chem. Soc.* 133, 6490–6492.
11. Gao, D., Zhou, H., Wang, J., Miao, S., Yang, F., Wang, G., Wang, J., and Bao, X. (2015). Size-dependent electrocatalytic reduction of CO<sub>2</sub> over Pd nanoparticles. *J. Am. Chem. Soc.* 137, 4288–4291.
12. Qiao, B., Wang, A., Yang, X., Allard, L.F., Jiang, Z., Cui, Y., Liu, J., Li, J., and Zhang, T. (2011). Single-atom catalysis of CO oxidation using Pt<sub>1</sub>/FeO<sub>x</sub>. *Nat. Chem.* 3, 634–641.
13. Ding, K., Gulec, A., Johnson, A.M., Schweitzer, N.M., Stucky, G.D., Marks, L.D., and Stair, P.C. (2015). Identification of active sites in CO oxidation and water-gas shift over supported Pt catalysts. *Science* 350, 189–192.
14. Lin, S., Diercks, C.S., Zhang, Y.-B., Kornienko, N., Nichols, E.M., Zhao, Y., Paris, A.R., Kim, D., Yang, P., and Yaghi, O.M. (2015). Covalent organic frameworks comprising cobalt porphyrins for catalytic CO<sub>2</sub> reduction in water. *Science* 349, 1208–1213.
15. Zhu, D.D., Liu, J.L., and Qiao, S.Z. (2016). Recent advances in inorganic heterogeneous



- electrocatalysts for reduction of carbon dioxide. *Adv. Mater.* **28**, 3423–3452.
16. Asadi, M., Kim, K., Liu, C., Addepalli, A.V., Abbasi, P., Yasaei, P., Phillips, P., Behranginia, A., Cerrato, J.M., and Haasch, R. (2016). Nanostructured transition metal dichalcogenide electrocatalysts for CO<sub>2</sub> reduction in ionic liquid. *Science* **353**, 467–470.
17. Wang, H., Jia, J., Song, P., Wang, Q., Li, D., Min, S., Qian, C., Wang, L., Li, Y.F., and Ma, C. (2017). Efficient electrocatalytic reduction of CO<sub>2</sub> by nitrogen-doped nanoporous carbon/carbon nanotube membranes—a step towards the electrochemical CO<sub>2</sub> refinery. *Angew. Chem. Int. Ed.* **56**, 7847–7852.
18. Lu, Z., Zhu, W., Yu, X., Zhang, H., Li, Y., Sun, X., Wang, X., Wang, H., Wang, J., and Luo, J. (2014). Ultrahigh hydrogen evolution performance of under-water “superaerophobic” MoS<sub>2</sub> nanostructured electrodes. *Adv. Mater.* **26**, 2683–2687.
19. He, J., Hu, B., and Zhao, Y. (2016). Superaerophobic electrode with metal@metal-oxide powder catalyst for oxygen evolution reaction. *Adv. Funct. Mater.* **26**, 5998–6004.
20. Lu, Z., Sun, M., Xu, T., Li, Y., Xu, W., Chang, Z., Ding, Y., Sun, X., and Jiang, L. (2015). Superaerophobic electrodes for direct hydrazine fuel cells. *Adv. Mater.* **27**, 2361–2366.
21. Jiang, K., Siahrostami, S., Akey, A.J., Li, Y., Lu, Z., Lattimer, J., Hu, Y., Stokes, C., Gangishetty, M., and Chen, G. (2017). Transition-metal single atoms in a graphene shell as active centers for highly efficient artificial photosynthesis. *Chem* **3**, 950–960.
22. Back, S., Lim, J., Kim, N.-Y., Kim, Y.-H., and Jung, Y. (2017). Single-atom catalysts for CO<sub>2</sub> electroreduction with significant activity and selectivity improvements. *Chem. Sci.* **8**, 1090–1096.
23. Yan, S., Li, Z., and Zou, Z. (2009). Photodegradation performance of g-C<sub>3</sub>N<sub>4</sub> fabricated by directly heating melamine. *Langmuir* **25**, 10397–10401.
24. Li, X., Bi, W., Chen, M., Sun, Y., Ju, H., Yan, W., Zhu, J., Wu, X., Chu, W., and Wu, C. (2017). Exclusive Ni-N<sub>4</sub> sites realize near-unity CO selectivity for electrochemical CO<sub>2</sub> reduction. *J. Am. Chem. Soc.* **139**, 14889–14892.
25. Trasobares, S., Stephan, O., Colliex, C., Hsu, W., Kroto, H., and Walton, D. (2002). Compartmentalized CN<sub>x</sub> nanotubes: chemistry, morphology, and growth. *J. Chem. Phys.* **116**, 8966–8972.
26. Wagner, R., and Ellis, W. (1964). Vapor-liquid-solid mechanism of single crystal growth. *Appl. Phys. Lett.* **4**, 89–90.
27. Givargizov, E. (1975). *Fundamental Aspects of VLS Growth. Vapour Growth and Epitaxy* (Elsevier), pp. 20–30.
28. Zhang, W., Jiang, X., Wang, X., Kaneti, Y.V., Chen, Y., Liu, J., Jiang, J.S., Yamauchi, Y., and Hu, M. (2017). Spontaneous weaving of graphitic carbon networks synthesized by pyrolysis of ZIF-67 crystals. *Angew. Chem. Int. Ed.* **56**, 8435–8440.
29. Qiu, H.-J., Ito, Y., Cong, W., Tan, Y., Liu, P., Hirata, A., Fujita, T., Tang, Z., and Chen, M. (2015). Nanoporous graphene with single-atom nickel dopants: an efficient and stable catalyst for electrochemical hydrogen production. *Angew. Chem. Int. Ed.* **54**, 14031–14035.
30. Fan, L., Liu, P.F., Yan, X., Gu, L., Yang, Z.Z., Yang, H.G., Qiu, S., and Yao, X. (2016). Atomically isolated nickel species anchored on graphitized carbon for efficient hydrogen evolution electrocatalysis. *Nat. Commun.* **7**, 10667.
31. Chen, Y., Ji, S., Wang, Y., Dong, J., Chen, W., Li, Z., Shen, R., Zheng, L., Zhuang, Z., and Wang, D. (2017). Isolated single iron atoms anchored on N-doped porous carbon as an efficient electrocatalyst for the oxygen reduction reaction. *Angew. Chem. Int. Ed.* **56**, 6937–6941.
32. Midgley, P., and Weyland, M. (2003). 3D electron microscopy in the physical sciences: the development of Z-contrast and EFTEM tomography. *Ultramicroscopy* **96**, 413–431.
33. Zheng, Y., Jiao, Y., Zhu, Y., Cai, Q., Vasileff, A., Li, L.H., Han, Y., Chen, Y., and Qiao, S.-Z. (2017). Molecule-level g-C<sub>3</sub>N<sub>4</sub> coordinated transition metals as a new class of electrocatalysts for oxygen electrode reactions. *J. Am. Chem. Soc.* **139**, 3336–3339.
34. Zhao, C., Dai, X., Yao, T., Chen, W., Wang, X., Wang, J., Yang, J., Wei, S., Wu, Y., and Li, Y. (2017). Ionic exchange of metal–organic frameworks to access single nickel sites for efficient electroreduction of CO<sub>2</sub>. *J. Am. Chem. Soc.* **139**, 8078–8081.
35. Li, C.W., and Kanan, M.W. (2012). CO<sub>2</sub> reduction at low overpotential on Cu electrodes resulting from the reduction of thick Cu<sub>2</sub>O films. *J. Am. Chem. Soc.* **134**, 7231–7234.
36. Dunwell, M., Lu, Q., Heyes, J.M., Rosen, J., Chen, J.G., Yan, Y., Jiao, F., and Xu, B. (2017). The central role of bicarbonate in the electrochemical reduction of carbon dioxide on gold. *J. Am. Chem. Soc.* **139**, 3774–3783.
37. Wuttig, A., Yoon, Y., Ryu, J., and Surendranath, Y. (2017). Bicarbonate is not a general acid in Au-catalyzed CO<sub>2</sub> electroreduction. *J. Am. Chem. Soc.* **139**, 17109–17113.
38. Kuhl, K.P., Hatsukade, T., Cave, E.R., Abram, D.N., Kibsgaard, J., and Jaramillo, T.F. (2014). Electrocatalytic conversion of carbon dioxide to methane and methanol on transition metal surfaces. *J. Am. Chem. Soc.* **136**, 14107–14113.
39. Nørskov, J.K., Rossmeisl, J., Logadottir, A., Lindqvist, L., Kitchin, J.R., Bligaard, T., and Jonsson, H. (2004). Origin of the overpotential for oxygen reduction at a fuel-cell cathode. *J. Phys. Chem. B* **108**, 17886–17892.